Two-pole structure of the $h_1(1415)$ axial-vector meson: resolving mass discrepancy

Samson Clymton[1, *] and Hyun-Chul Kim[1, 2, †]

[1]*Department of Physics, Inha University, Incheon 22212, Republic of Korea*
[2]*School of Physics, Korea Institute for Advanced Study (KIAS), Seoul 02455, Republic of Korea*
(Dated: September 5, 2024)

We investigate isoscalar axial-vector mesons using a coupled-channel formalism. The kernel amplitudes are constructed from meson-exchange diagrams in the t- and u-channels, which are derived from effective Lagrangians based on hidden local symmetry. We incorporate six channels: $\pi\rho$, $\eta\omega$, $K\bar{K}^*$, $\eta\phi$, $\eta'\omega$, and $\eta'\phi$, and solve the off-shell coupled integral equations. We first discuss the dynamical generation of the $h_1(1170)$. The pole diagram for $h_1(1595)$ has a certain effect on the generation of $h_1(1170)$. We observe two poles at $(1387-i6)$ MeV and $(1452-i51)$ MeV, which exhibit a two-pole structure of the $h_1(1415)$ meson. This two-pole structure may resolve the discrepancy in the experimental data on the mass of $h_1(1415)$. The results show that the lower pole couples strongly to the $K\bar{K}^*$ channel, while the higher pole couples predominantly to the $\eta\phi$ channel. This provides insights into the nature of h_1 mesons and explains possible discrepancies in the mass of $h_1(1415)$.

I. INTRODUCTION

Recently, the BESIII Collaboration reported new data on the excited $h_1(1415)$ meson with quantum numbers $I^G(J^{PC}) = 0^-(1^{+-})$, based on a partial-wave analysis of $J/\psi \to \gamma\eta'\eta'$. They found its mass to be $m_{h_1(1415)} = (1384\pm6^{+9}_{-0})$ MeV and width $\Gamma = (66\pm10^{+12}_{-10})$ MeV [1]. These new results are consistent with the earliest measurements of $h_1(1415)$[2], which reported $m_{h_1(1415)} = (1380 \pm 20)$ MeV and $\Gamma = (80 \pm 30)$ MeV from the $K^-p \to K_S^0\bar{K}\pi\Lambda$ process. However, they differ from several other experimental findings. The Crystal Barrel experiment[3] measured respectively its mass and width as (1440 ± 60) MeV and (170 ± 80) MeV from $p\bar{p} \to K_L K_S \pi^0\pi^0$. An earlier BESIII experiment [4] found $m = (1412 \pm 12)$ MeV and $\Gamma = (84 \pm 52)$ MeV from $\chi_{1,2,J} \to \phi K\bar{K}\pi$. In 2018, BESIII [5] reported $m = (1423.2 \pm 9.4)$ MeV and $\Gamma = (90.3 \pm 27.3)$ MeV from $J/\psi \to \eta'K\bar{K}\pi$, with interference effects yielding $m = (1441.7 \pm 4.9)$ MeV and $\Gamma = (111.5 \pm 12.8)$ MeV. Notably, the $K\bar{K}^*$ threshold energy ($E_{\rm th}^{K\bar{K}^*} \approx 1390$ MeV) lies between the $h_1(1415)$ masses reported in Refs.[1, 2] and those in Refs.[3–5]. It is crucial to understand the origin of these discrepancies. While $h_1(1415)$ decays primarily into $K\bar{K}^*$, other channels near its mass likely contribute as well. The lowest $h_1(1170)$ state decays into $\pi\rho$, suggesting this channel may also affect $h_1(1415)$ production.

The Particle Data Group (PDG) classifies the h_1 mesons as isoscalar $q\bar{q}$ states, i.e. $c_1(u\bar{u} + d\bar{d}) + c_2 s\bar{s}$ like η, η', ω, and ϕ [6]. This indicates that the h_1 mesons are considered to be orbitally excited states as the isoscalar pseudoscalar or vector mesons with the same quark content. Similarly, the $a_1(1260)$ isovector axial-vector meson is also regarded as the isovector $q\bar{q}$ state. However, a series of studies suggests that the $a_1(1260)$ meson may be a possible molecular state [7–11]. Very recently, we have investigated the b_1 isovector axial-vector mesons, demonstrating that they can be dynamically generated by considering the four different channels, i.e. $\pi\omega$, $\eta\rho$, $\pi\phi$, and $K\bar{K}^*$ channels. Interestingly, it was shown that the $b_1(1235)$ arises from the $b_1(1306)$ and $b_1(1356)$ [12], indicating that the $b_1(1235)$ has a two pole structure. As will be shown in the current work, the $h_1(1415)$ meson originates from the two poles: $h_1(1387)$ and $h_1(1452)$. In fact, various hadrons exhibit the two-pole structures. For example, the $K_1(1270)$ may possibly be regarded as the meson with the two-pole structure [8, 13]. Albaladejo et al. [14] showed that the $D^*(2400)$ arises as a two-pole structure, based on light pseudoscalar and D meson interactions in the coupled-channel formalism (see a recent review [15] for detailed discussion). The two-pole structure is also found in the baryonic sector: $\Lambda(1405)$ is now well established as the hyperon with the two-pole structure [6, 16–18].

In the present work, we will show that the discrepancy in the experimental data on the mass of $h_1(1415)$ is rooted in its two-pole structure. To this end, we formulate the off-shell coupled-channel formalism [11, 12, 19], introducing six different channels, i.e. $\pi\rho$, $\eta\omega$, $K\bar{K}^*$, $\eta\phi$, $\eta'\omega$, and $\eta'\phi$ of which the threshold energies lie below 2 GeV. We first construct the kernel amplitude corresponding to each channel, using the meson-exchange diagrams. We compute the coupled Blankenbecler-Sugar (BbS) equations, which are obtained from the three-dimensional (3D) reduction of the

Bethe-Salpeter equations [20, 21]. We have already investigated how the $a_1(1260)$ and $b_1(1235)$ axial-vector mesons, $D_{s0}^*(2317)$ and B_{s0}^* mesons, and the hidden charm pentaquark states are generated dynamically within the same framework [11, 12, 19, 22]. We will demonstrate that the $h_1(1170)$ and $h_1(1415)$ are dynamically generated even without introducing the corresponding pole diagrams. Remarkably, the two poles emerge in the second Riemann sheet, which are related to the $h_1(1415)$ meson, of which one lies just below the $K\bar{K}^*$ threshold, and the other is found to have a larger mass than its threshold energy.

The outline of the current work is sketched as follows: In Section II, we first explain how the kernel amplitude for each channel can be constructed by using the Feynman diagrams based on the effective Lagrangian. Then, we perform the partial-wave expansion for the coupled BbS integral equations, so that we examine the relevant partial waves with proper quantum numbers corresponding to the h_1 mesons. In Section III, we discuss the results for the h_1 mesons. We examine the role of each channel in producing them dynamically. In particular, we focus on the two-pole structure of the $h_1(1415)$ meson. The last section summarizes the present work.

II. GENERAL FORMALISM

The scattering amplitude is defined as

$$\mathcal{S}_{fi} = \delta_{fi} - i(2\pi)^4 \delta(P_f - P_i)\mathcal{T}_{fi}, \tag{1}$$

where P_i and P_f stand for the total four momenta of the initial and final states, respectively. The transition amplitude $\mathcal{T}_{fi}$ for a two-body reaction can be derived from the Bethe-Salpeter integral equations

$$\mathcal{T}_{fi}(p',p;s) = \mathcal{V}_{fi}(p',p;s) + \frac{1}{(2\pi)^4}\sum_k \int d^4q \mathcal{V}_{fk}(p',q;s)\mathcal{G}_k(q;s)\mathcal{T}_{ki}(q,p;s), \tag{2}$$

where p and p' denote the relative four-momentum of the initial and final states, respectively. q is the momentum transfer for the intermediate states in the center of mass (CM) frame. s represents the square of the total energy, which is just one of the Mandelstam variables, $s = P_i^2 = P_f^2$. The coupled integral equations given in Eq. (2) can be illustrated as in Fig. 1. The summation Σ represents the inclusion of various coupled channels. To avoid the
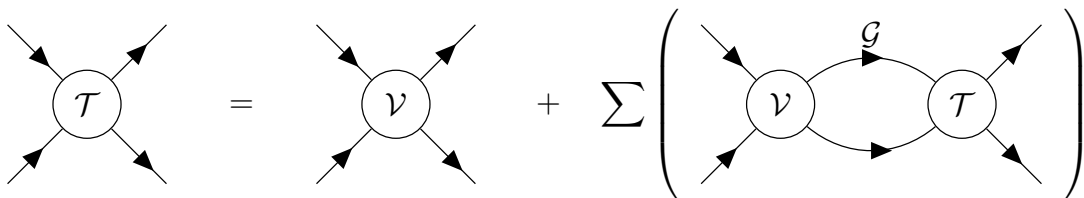

Figure 1. Graphical representation of the coupled integral scattering equation.

complexity due to the four-dimensional integral equations, we make a 3D reduction. Among several methods for the 3D reduction, we employ the BbS scheme [20, 21], which expresses the two-body propagator in the form of

$$\mathcal{G}_k(q) = \delta\left(q_0 - \frac{E_{k1}(\boldsymbol{q}) - E_{k2}(\boldsymbol{q})}{2}\right)\frac{\pi}{E_{k1}(\boldsymbol{q})E_{k2}(\boldsymbol{q})}\frac{E_k(\boldsymbol{q})}{s - E_k^2(\boldsymbol{q})}. \tag{3}$$

Here, E_k represents the total on-mass-shell energy of the intermediate state, $E_k = E_{k1} + E_{k2}$, and $\boldsymbol{q}$ designates the three-momentum transfer of the intermediate state. Utilizing Eq. (3), we obtain the following coupled BbS integral equations

$$\mathcal{T}_{fi}(\boldsymbol{p}',\boldsymbol{p}) = \mathcal{V}_{fi}(\boldsymbol{p}',\boldsymbol{p}) + \frac{1}{(2\pi)^3}\sum_k \int \frac{d^3\boldsymbol{q}}{2E_{k1}(\boldsymbol{q})E_{k2}(\boldsymbol{q})}\mathcal{V}_{fk}(\boldsymbol{p}',\boldsymbol{q})\frac{E_k(\boldsymbol{q})}{s - E_k^2(\boldsymbol{q}) + i\varepsilon}\mathcal{T}_{ki}(\boldsymbol{q},\boldsymbol{p}), \tag{4}$$

where $\boldsymbol{p}$ and $\boldsymbol{p}'$ are the relative three-momenta of the initial and final states in the CM frame, respectively. In this manner, the T matrix can be generated, the entire Hilbert space being considered with the off-shell components.

Before we solve the coupled BbS integral equations, we need to construct the kernel amplitudes $\mathcal{V}$. We compute $\mathcal{V}_{fi}$ by using the effective Lagrangians for the meson-meson interactions. Since the vector mesons are involved, we

consider hidden local symmetry, where the vector meson is considered as a dynamic gauge boson [23, 24]. In Ref. [24], the effective interactions among vector, vector, and pseudoscalar mesons were derived, based on the SU(3) hidden local symmetry. The effective Lagrangians are then expressed as

$$\mathcal{L}_{PPV} = -ig_{PPV}\sqrt{2}\,\text{Tr}\left([P,\partial_\mu P]\,V^\mu\right),$$
$$\mathcal{L}_{VVV} = ig_{VVV}\sqrt{2}\,\text{Tr}\left((\partial_\mu V_\nu - \partial_\nu V_\mu)V^\mu V^\nu\right),$$
$$\mathcal{L}_{PVV} = -\frac{g_{PVV}}{m_V}\sqrt{2}\,\varepsilon^{\mu\nu\alpha\beta}\text{Tr}\left(\partial_\mu V_\nu \partial_\alpha V_\beta P\right), \tag{5}$$

where P and V represent respectively the pseudoscalar and vector matrices in flavor space

$$P = \begin{pmatrix} \frac{1}{\sqrt{2}}\pi^0 + \frac{1}{\sqrt{6}}\eta_8 + \frac{1}{\sqrt{2}}\eta_1 & \pi^+ & K^+ \\ \pi^- & -\frac{1}{\sqrt{2}}\pi^0 + \frac{1}{\sqrt{6}}\eta_8 + \frac{1}{\sqrt{2}}\eta_1 & K^0 \\ K^- & \bar{K}^0 & -\frac{2}{\sqrt{6}}\eta_8 + \frac{1}{\sqrt{2}}\eta_1 \end{pmatrix},$$

$$V = \begin{pmatrix} \frac{1}{\sqrt{2}}\rho_\mu^0 + \frac{1}{\sqrt{2}}\omega_\mu & \rho_\mu^+ & K_\mu^{*+} \\ \rho_\mu^- & -\frac{1}{\sqrt{2}}\rho_\mu^0 + \frac{1}{\sqrt{2}}\omega_\mu & K_\mu^{*0} \\ K_\mu^{*-} & \bar{K}_\mu^{*0} & \phi_\mu \end{pmatrix}. \tag{6}$$

We assume the ideal mixing of the isoscalar vector meson singlet and octet. For η and η', we define them in terms of the pseudoscalar octet η_8 and singlet η_1:

$$\eta = \eta_8 \cos\theta_P - \eta_1 \sin\theta_P, \quad \eta' = \eta_8 \sin\theta_P + \eta_1 \cos\theta_P, \tag{7}$$

with mixing angle $\theta_P = -17°$ taken from Ref. [25]. Note that the universal coupling constant is given as $g = g_{PPV} = g_{VVV}$ due to the hidden local symmetry.

As done in the previous works [11, 12, 19], we consider the five different isoscalar axial-vector channels coupled to the $\pi\rho$ channel, which are relevant to the h_1 mesons, i.e., the $\eta\omega$, $K\bar{K}^*$, $\eta\phi$, $\eta'\omega$, and $\eta'\phi$ channels. Thus, the kernel matrix is now expressed as

$$\mathcal{V} = \begin{pmatrix} \mathcal{V}_{\pi\rho\to\pi\rho} & \mathcal{V}_{\eta\omega\to\pi\rho} & \mathcal{V}_{K\bar{K}^*\to\pi\rho} & \mathcal{V}_{\eta\phi\to\pi\rho} & \mathcal{V}_{\eta'\omega\to\pi\rho} & \mathcal{V}_{\eta'\phi\to\pi\rho} \\ \mathcal{V}_{\pi\rho\to\eta\omega} & \mathcal{V}_{\eta\omega\to\eta\omega} & \mathcal{V}_{K\bar{K}^*\to\eta\omega} & \mathcal{V}_{\eta\phi\to\eta\omega} & \mathcal{V}_{\eta'\omega\to\eta\omega} & \mathcal{V}_{\eta'\phi\to\eta\omega} \\ \mathcal{V}_{\pi\rho\to K\bar{K}^*} & \mathcal{V}_{\eta\omega\to K\bar{K}^*} & \mathcal{V}_{K\bar{K}^*\to K\bar{K}^*} & \mathcal{V}_{\eta\phi\to K\bar{K}^*} & \mathcal{V}_{\eta'\omega\to K\bar{K}^*} & \mathcal{V}_{\eta'\phi\to K\bar{K}^*} \\ \mathcal{V}_{\pi\rho\to\eta\phi} & \mathcal{V}_{\eta\omega\to\eta\phi} & \mathcal{V}_{K\bar{K}^*\to\eta\phi} & \mathcal{V}_{\eta\phi\to\eta\phi} & \mathcal{V}_{\eta'\omega\to\eta\phi} & \mathcal{V}_{\eta'\phi\to\eta\phi} \\ \mathcal{V}_{\pi\rho\to\eta'\omega} & \mathcal{V}_{\eta\omega\to\eta'\omega} & \mathcal{V}_{K\bar{K}^*\to\eta'\omega} & \mathcal{V}_{\eta\phi\to\eta'\omega} & \mathcal{V}_{\eta'\omega\to\eta'\omega} & \mathcal{V}_{\eta'\phi\to\eta'\omega} \\ \mathcal{V}_{\pi\rho\to\eta'\phi} & \mathcal{V}_{\eta\omega\to\eta'\phi} & \mathcal{V}_{K\bar{K}^*\to\eta'\phi} & \mathcal{V}_{\eta\phi\to\eta'\phi} & \mathcal{V}_{\eta'\omega\to\eta'\phi} & \mathcal{V}_{\eta'\phi\to\eta'\phi} \end{pmatrix} \tag{8}$$

Each matrix element $\mathcal{V}_{fi}$ is obtained from the corresponding tree-level Feynman diagram illustrated in Fig. 2. Note
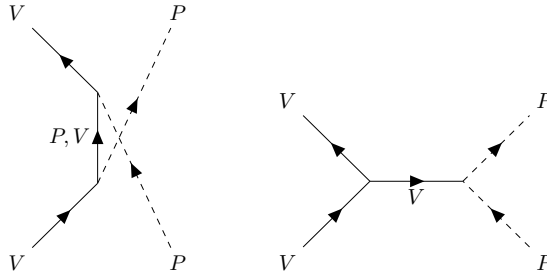

Figure 2. Meson-exchange diagrams in the u- and t-channels are depicted in the left and right panels, respectively. P and V stand for the pseudoscalar and vector mesons.

that we do not have any pole diagrams in the s-channel, which indicates that the $h_1(1170)$ and $h_1(1415)$ mesons will be dynamically generated. However, the $h_1(1595)$ meson requires the s-channel pole digram, which we will discuss later its physical implications. The Feynman amplitudes for the tree-level diagrams are evaluated from the effective Lagrangians given in Eq.(5). Imposing flavor SU(3) symmetry for the coupling constants, we find that the following kernel amplitudes become null: $\mathcal{V}_{\pi\rho\to\eta\phi}$, $\mathcal{V}_{\pi\rho\to\eta'\phi}$, $\mathcal{V}_{\eta\omega\to\eta\phi}$, $\mathcal{V}_{\eta\omega\to\eta'\phi}$, $\mathcal{V}_{\eta\phi\to\eta'\omega}$ and $\mathcal{V}_{\eta'\omega\to\eta'\phi}$.

The amplitudes of the meson exchange diagrams shown in Fig. 2 from left to right are written as

$$\mathcal{A}_P^u(\boldsymbol{p}',\boldsymbol{p}) = -\,\mathrm{IS}\,g_{PPV}^2\,F^2(\boldsymbol{p},\boldsymbol{p}')\,(2p_2 - p_3)\cdot\epsilon^*\mathcal{P}(p_1 - p_4)\,(2p_4 - p_1)\cdot\epsilon, \tag{9}$$

$$\mathcal{A}_V^u(\boldsymbol{p}',\boldsymbol{p}) = -\,\mathrm{IS}\,\frac{g_{PVV}^2}{m_V^2}\,F^2(\boldsymbol{p},\boldsymbol{p}')\,\varepsilon_{\mu\nu\alpha\beta}\,p_3^\mu\epsilon^{*\nu}(p_3 - p_2)^\alpha\,\mathcal{P}^{\beta\delta}(p_1 - p_4)\,\varepsilon_{\gamma\sigma\eta\delta}p_1^\gamma\epsilon^\sigma(p_1 - p_4)^\eta, \tag{10}$$

$$\mathcal{A}_V^t(\boldsymbol{p}',\boldsymbol{p}) = -\,\mathrm{IS}\,g_{PPV}^2\,F^2(\boldsymbol{p},\boldsymbol{p}')\,(p_2 + p_4)^\mu\,\mathcal{P}_{\mu\nu}(p_1 - p_3)$$
$$\times\,[(2p_1 - p_3)\cdot\epsilon^*\epsilon^\nu + (2p_3 - p_1)\cdot\epsilon\epsilon^{*\nu} - \epsilon\cdot\epsilon^*(p_1 + p_3)^\nu]\,, \tag{11}$$

where the IS factor is related to the corresponding SU(3) Clebsch-Gordan coefficient and isospin factor. In Table I, we list the values of the IS factors for all relevant processes. For the coupling constants, we use the values for the coupling constants: $g_{PPV}^2/4\pi = 0.72$ and $g_{PVV}^2/4\pi = 1.88$ from the previous works [11, 12]. The propagators for the spin-0 and spin-1 mesons are expressed by

$$\mathcal{P}(p) = \frac{1}{p^2 - m^2}, \quad \mathcal{P}_{\mu\nu}(p) = \frac{1}{p^2 - m^2}\left(-g_{\mu\nu} + \frac{p_\mu p_\nu}{m^2}\right), \tag{12}$$

where m denotes the mass corresponding to the exchange meson. As done in the previous works [11, 12], we have turned off the energy-dependence in the denominator of the propagator.

Table I. The IS factors and cutoff parameters (Λ_0) in unit of MeV for each reaction.

Reaction	Exchange meson	Type	IS	Λ_0(MeV)
$\pi\rho \to \pi\rho$	π	u	-8	600
	ρ	t	-8	600
	ω	u	4	600
$\pi\rho \to \eta\omega$	ρ	u	-5.48	1550
$\pi\rho \to K\bar{K}^*$	K	u	$\sqrt{6}$	700
	K^*	t	$\sqrt{6}$	750
$\pi\rho \to \eta'\omega$	ρ	u	-4.24	1600
$\eta\omega \to \eta\omega$	ω	u	2.50	600
$\eta\omega \to K\bar{K}^*$	K	u	-2.34	600
	K^*	t	-2.34	700
$\eta\omega \to \eta'\omega$	ω	u	1.94	600
$K\bar{K}^* \to K\bar{K}^*$	ρ	t	-3	600
	ω	t	-1	600
	ϕ	t	-2	1400
$K\bar{K}^* \to \bar{K}K^*$	π	u	3	600
	η	u	2.74	600
	ρ	u	-3	600
	ω	u	-1	600
	ϕ	u	-2	1400
$K\bar{K}^* \to \eta\phi$	K	u	-3.31	600
	K^*	t	-3.31	1710
$K\bar{K}^* \to \eta'\omega$	K	u	0.72	600
	K^*	t	0.72	700
$K\bar{K}^* \to \eta'\phi$	K	u	1.01	600
	K^*	t	1.01	1700
$\eta\phi \to \eta\phi$	ϕ	u	3.00	600
$\eta\phi \to \eta'\phi$	ϕ	u	-3.87	600
$\eta'\omega \to \eta'\omega$	ω	u	1.50	600
$\eta'\phi \to \eta'\phi$	ϕ	u	5.00	600

Since hadrons have finite sizes, we introduce a form factor at each vertex. We employ the following parametrization [26]:

$$F(\boldsymbol{p},\boldsymbol{p}') = \left(\frac{n\Lambda^2 - m^2}{n\Lambda^2 + \boldsymbol{p}^2 + \boldsymbol{p}'^2}\right)^n, \tag{13}$$

where n is the power of the form factor. The form given in Eq. (13) has a notable advantage: the value of Λ remains constant regardless of change in n. As n approaches infinity, Eq. (13) converges to a Gaussian form. In most cases,

we use $n = 1$. However, we need to use $n = 2$ for vector-meson exchange, because they have stronger momentum dependence. While the cut-off masses Λ in Eq. (13) are experimentally unknown for the current hadronic processes, we minimize associated uncertainties using the following strategy as done in the previous works [11, 12, 19]: we choose Λ by adding approximately $(500 - 700)$ MeV to the corresponding masses of the exchange meson. Consequently, we define the cutoff mass as $\Lambda = \Lambda_0 + m$. We set Λ_0 to be 600 MeV for most cases, as listed in Table. I. However, to fit the total cross section for $\pi\rho$ scattering, we need to use larger values of Λ_0 for some of the vector-meson exchange diagrams, as shown in Table I.

To compute the coupled integral equations, we utilize a partial wave decomposition, transforming the equation into a one-dimensional integral equation as follows

$$\mathcal{T}_{\lambda'\lambda}^{J(fi)}(\mathrm{p}',\mathrm{p}) = \mathcal{V}_{\lambda'\lambda}^{J(fi)}(\mathrm{p}',\mathrm{p}) + \frac{1}{(2\pi)^3}\sum_{k,\lambda_k}\int \frac{\mathrm{q}^2 d\mathrm{q}}{2E_{k1}E_{k2}}\mathcal{V}_{\lambda'\lambda_k}^{J(fk)}(\mathrm{p}',\mathrm{q})\frac{E_k}{s-E_k^2}\mathcal{T}_{\lambda_k\lambda}^{J(ki)}(\mathrm{q},\mathrm{p}). \tag{14}$$

Here, λ', λ and λ_k denote the relative helicity of the final, initial and intermediate two-body states, respectively. Their corresponding momenta are represented by p', p and q, respectively. The partial-wave component is given by

$$\mathcal{V}_{\lambda'\lambda}^{J(fi)}(\mathrm{p}',\mathrm{p}) = 2\pi \int d(\cos\theta)\,d_{\lambda',\lambda}^{J}(\theta)\,\mathcal{V}_{\lambda'\lambda}^{fi}(\mathrm{p}',\mathrm{p},\theta), \tag{15}$$

where θ stands for the scattering angle, and $d_{\lambda',\lambda}^{J}$ are the Wigner d-matrices.

To obtain the transition amplitudes numerically, it is crucial to deal with the singularities in the BbS propagator. The one-dimensional integral, free from energy singularities, takes the form

$$\mathcal{T}_{\lambda'\lambda}^{fi}(\mathrm{p}',\mathrm{p}) = \mathcal{V}_{\lambda'\lambda}^{fi}(\mathrm{p}',\mathrm{p}) + \frac{1}{(2\pi)^3}\sum_{k,\lambda_k}\left[\int_0^\infty d\mathrm{q}\frac{\mathrm{q}E_k}{E_{k1}E_{k2}}\frac{\mathcal{F}(\mathrm{q})-\mathcal{F}(\tilde{\mathrm{q}}_k)}{s-E_k^2} + \frac{1}{2\sqrt{s}}\left(\ln\left|\frac{\sqrt{s}-E_k^{\mathrm{thr}}}{\sqrt{s}+E_k^{\mathrm{thr}}}\right| - i\pi\right)\mathcal{F}(\tilde{\mathrm{q}}_k)\right], \tag{16}$$

where $\tilde{\mathrm{q}}_k$ represents the momentum when $E_{k1} + E_{k2} = \sqrt{s}$ and $\mathcal{F}(\mathrm{q})$ is defined as

$$\mathcal{F}(\mathrm{q}) = \frac{1}{2}\mathrm{q}\,\mathcal{V}_{\lambda'\lambda_k}^{fk}(\mathrm{p}',\mathrm{q})\mathcal{T}_{\lambda_k\lambda}^{ki}(\mathrm{q},\mathrm{p}). \tag{17}$$

Regularization is applied only when the total energy $\sqrt{s}$ surpasses the threshold energy of the k-th channel, denoted as E_k^{thr}. Notably, the transition amplitudes derived from these equations can be analytically continued to the complex energy plane directly, as the energy singularities have been eliminated. Moreover, Eq. 16 enables the use of the matrix inversion method to compute the transition amplitudes. The partial-wave transition amplitudes are then obtained by transforming the helicity basis into the LSJ basis. For the specific case of pseudoscalar and vector meson scattering, this transformation is represented as

$$\mathcal{T}_{L'L}^{JS} = \frac{\sqrt{(2L+1)(2L'+1)}}{2J+1}\sum_{\lambda'\lambda}\left(L'0S\lambda'|J\lambda'\right)\left(1\lambda'00|1\lambda'\right)\left(L0S\lambda|J\lambda\right)\left(1\lambda00|S\lambda\right)\mathcal{T}_{\lambda',\lambda}^{J}. \tag{18}$$

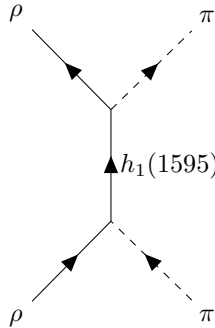Here, $(j_1 m_1 j_2 m_2|JM)$ denotes the Clebsch-Gordan coefficient.

Figure 3. $h_1(1595)$ pole diagram in the $\pi\rho$ elastic scattering.

So far, we have focused on using only the t and u channel exchange diagrams. However, it is necessary to include the pole diagram for the $h_1(1595)$ meson in the s channel. It is essential to improve the results in comparison with the experimental data on $\pi\rho$ scattering. A similar approach was demonstrated in the case of $\pi\pi$ scattering [27], where the explicit inclusion of the $f_0(1400)$ pole was necessary to reproduce the experimental phase shift of the scalar-isoscalar channel in the energy region below 2 GeV. The presence of $f_0(1400)$ influenced both the high-energy region and the structure below 1 GeV. Similarly, we incorporate the s-channel pole diagram for $h_1(1595)$ in $\pi\rho$ scattering, as illustrated in Fig. 3. The interaction vertices are determined by the following effective Lagrangian

$$\mathcal{L}_{h_1\pi\rho} = \frac{g_{h_1\pi\rho}}{m_{h_1}^0} \left(\partial_\mu\rho_\nu - \partial_\nu\rho_\mu\right)\pi\partial^\mu h_1^\nu. \tag{19}$$

The bare mass and coupling of $h_1(1595)$ are set to be $m_{h_1(1595)}^{(0)} = 1320$ MeV and $g_{h_1(1595)\pi\rho}^2/4\pi = 0.54$. Additionally, we employ the form factor in the s channel

$$F_s(\boldsymbol{p}) = \left(\frac{\Lambda^2 + (m_{h_1}^0)^2}{\Lambda^2 + \boldsymbol{p}^2}\right)^4, \tag{20}$$

to ensure that the contribution of the pole diagram in the high momentum region is negligible. Consequently, the pole diagram has a small impact on the dynamical generation of the h_1 meson. We set the cutoff mass, denoted as Λ, to be 1920 MeV, following the previously mentioned rule. As a result, the dressed mass and width of $h_1(1595)$ evaluated in the complex energy plane match the PDG average value [6]. We found the u-channel contribution to the transition amplitude to be negligible and omitted it for simplicity. The t-channel diagram is not allowed due to G parity and isospin symmetry. The necessity of including the pole diagram suggests that the $h_1(1595)$ may be predominantly a genuine $q\bar{q}$ state.

III.   RESULTS AND DISCUSSIONS

A. h_1 resonances

The ground state of the h_1 axial-vector meson was first observed in the 3π mass spectra of the charge exchange reaction $\pi^-p \to \pi^+\pi^-\pi^0n$ [28]. Its existence was later confirmed by only one other experiment using the same reaction [29]. According to the PDG, there are two excited states of h_1 meson: $h_1(1415)$ and $h_1(1595)$ [6]. The latter was observed in the $\eta\omega$ mass distribution [30], while the former exhibits an intriguing structure similar to the renowned $\Lambda(1405)$. Initially, referred to as $h_1(1380)$, subsequent experimental studies determined its mass to be approximately $1.42 - 1.44$ GeV, leading to its renaming as $h_1(1415)$. However, a very recent experiment again suggests that the mass of $h_1(1415)$ is roughly 1.38 GeV. Currently, there is no explanation for the conflicting mass measurements of $h_1(1415)$. Interestingly, $h_1(1380)$ is located just below the $K\bar{K}^*$ threshold, whereas the renamed $h_1(1415)$ is found to be above $K\bar{K}^*$ threshold. This implies that $h_1(1380)$ ($h_1(1415)$) may have a two-pole structure. In this work, we will examine each h_1 meson within the coupled-channel framework. Specifically, we will demonstrate that the conflicting mass measurements of $h_1(1415)$ can be explained by a two-pole structure.

In Ref. [28], two axial-vector resonances, a_1 and h_1, were identified in the charge exchange reaction. Previously, we analyzed experimental data on the former one, and in this current study, we extend our analysis to the latter one, keeping values of the parameters the same as the earlier investigation [11]. The assumption of mixing between η and η' alters the isospin value of η exchange in the $K\bar{K}^*$ elastic channel. However, the mixing has a negligible effect on the previous results for the a_1 meson, given the fact that η exchange barely contributes to $K\bar{K}^*$ elastic scattering.

To describe the experimental data in the isoscalar channel, we relate the total cross section to the transition amplitude $\mathcal{T}$ using a constant factor C, expressed as

$$\sigma \equiv -C\operatorname{Im}\left[\mathcal{T}_{\pi\rho}(M_{\pi\rho})\right], \tag{21}$$

where C has a different value from that in the isovector channel due to the absorption of the isospin factor into C. The pole diagram for $h_1(1595)$ comes into essential play in enhancing the width of $h_1(1170)$, resulting in good agreement with the experimental data. The total cross section for $\pi\rho$ scattering in the isoscalar channel clearly reveals the resonance of the $h_1(1170)$ meson, of which the mass and width are determined to be $m_{h_1(1170)} = (1.19 \pm 0.06)$ GeV and $\Gamma = (0.32 \pm 0.05)$ GeV, respectively [28]. The present results describe the experimental data well. We also compare them with those in Ref. [31] that utilized a single $\pi\rho$ channel including explicitly the $h_1(1170)$ pole diagram. As shown in Fig. 4, the single channel with the explicit pole of the $h_1(1170)$ is insufficient to describe the experimental
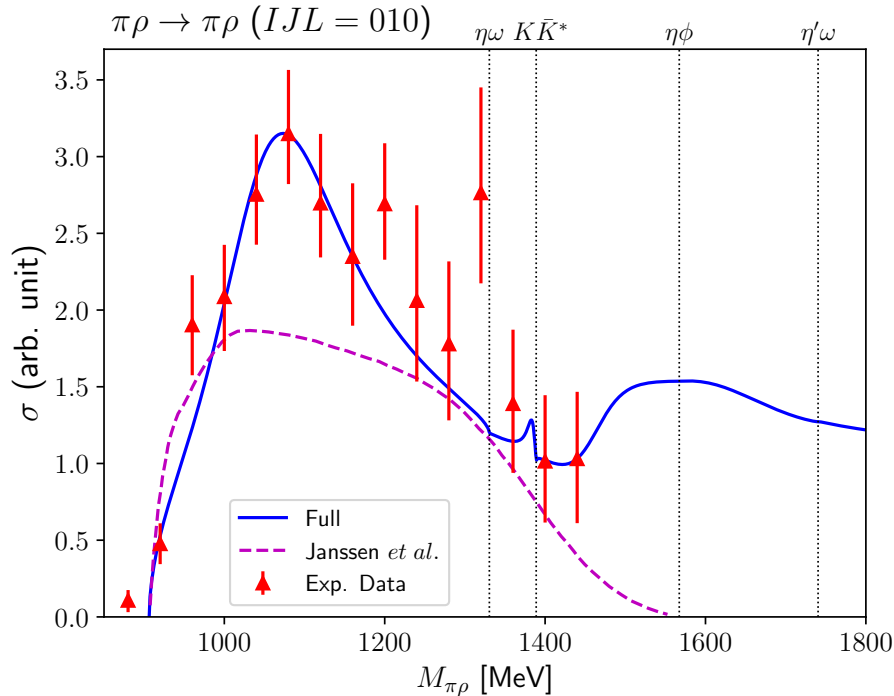
Figure 4. Total cross section for $\pi\rho$ scattering in the $IJL = 010$ channel as a function of the $\pi\rho$ invariant mass. The solid curve depicts the present results, whereas the dashed one draws that from Ref. [31]. The experimental data are taken from Ref. [28].

data, specifically the $h_1(1170)$ peak structure. In contrast, we find that the $h_1(1595)$ pole diagram has an important contribution to explain the $h_1(1170)$ resonance. Moreover, various coupled channels play essential roles in dynamically generating the h_1 (1170) resonance. The dynamical generation of h_1 (1170) has also been observed in Ref. [8]. So, we conclude that the $h_1(1170)$ does not solely originate from the $q\bar{q}$ state but contains a substantial component of the molecular state. Furthermore, we predict a small peak structure near the $K\bar{K}^*$ threshold, which is barely seen in the experimental data.

To identify dynamically generated resonances in the current approach, we examine the T amplitude in the second Riemann sheet. Since the T amplitude generated by Eq. (16) is a meromorphic function in the complex energy plane, we can directly identify the h_1 resonances in the second Riemann sheet. In Fig. 5, the contour plot of the modulus of T clearly exhibits the existence of four poles. The first pole below the $\eta\omega$ threshold is positioned at $(1080 - i118)$ MeV, so its mass and width are respectively given as 1080 MeV and 236 MeV. The value of the width given in the PDG is (375 ± 35) MeV [6], which was taken from the fit by using the Bowler model. Compared with it, the current result is smaller than the empirical data. In Ref. [8], the corresponding pole for $h_1(1170)$ was found at $\sqrt{s} = (919 - i17)$ MeV, which deviates significantly from the experimental data. The second and third poles are located at $(1387 - i6)$ MeV and $(1452 - i51)$ MeV, respectively. These two poles are related to $h_1(1415)$, once called as $h_1(1380)$. Since the second pole lies just below the $K\bar{K}^*$ threshold, it may be considered as the $K\bar{K}^*$ molecular state in the isoscalar channel. Interestingly, its width is very small. The third pole is located at about 60 MeV above the $K\bar{K}^*$ threshold, and its width is 102 MeV. While the average value from the PDG is given as (78 ± 11) MeV, the experimental data on its width ranges from $(66 \pm 10^{+12}_{-10})$ MeV [1] to (170 ± 80) MeV [3]. Thus, the width of $h_1(1415)$ should be measured more precisely. If $h_1(1415)$ has a two-pole structure, its width may be determined more precisely.

Finally, the fourth pole is observed at $(1603 - i158)$ MeV that corresponds to the $h_1(1595)$ meson, placed above the $\eta\phi$ threshold. Note that we have included the pole diagram for $h_1(1595)$ in the s channel with the bare mass $m^{(0)}_{h_1(1595)} = 1320$ MeV. It is dressed to be 1603 MeV, as the pole diagram for $h_1(1595)$ is "*renormalized*" by the coupled integral equations. When considering only the $\pi\rho$ elastic channel, the dressed mass is smaller than the bare one. However, the pole diagram gains additional mass after being coupled to all channels. A similar effect is observed in $\pi\pi$ elastic scattering, where the scalar-isoscalar meson $f_0(1400)$ has a bare mass of 1300 MeV with the scalar coupling, and after coupling to other channels, the physical mass becomes 1400 MeV [27]. While a recent study shows that the $h_1(1595)$ is a ground state of a light tetraquark state [32], the current result suggests that the structure of the $h_1(1595)$ has a large component of the $q\bar{q}$, being dressed by various channels.
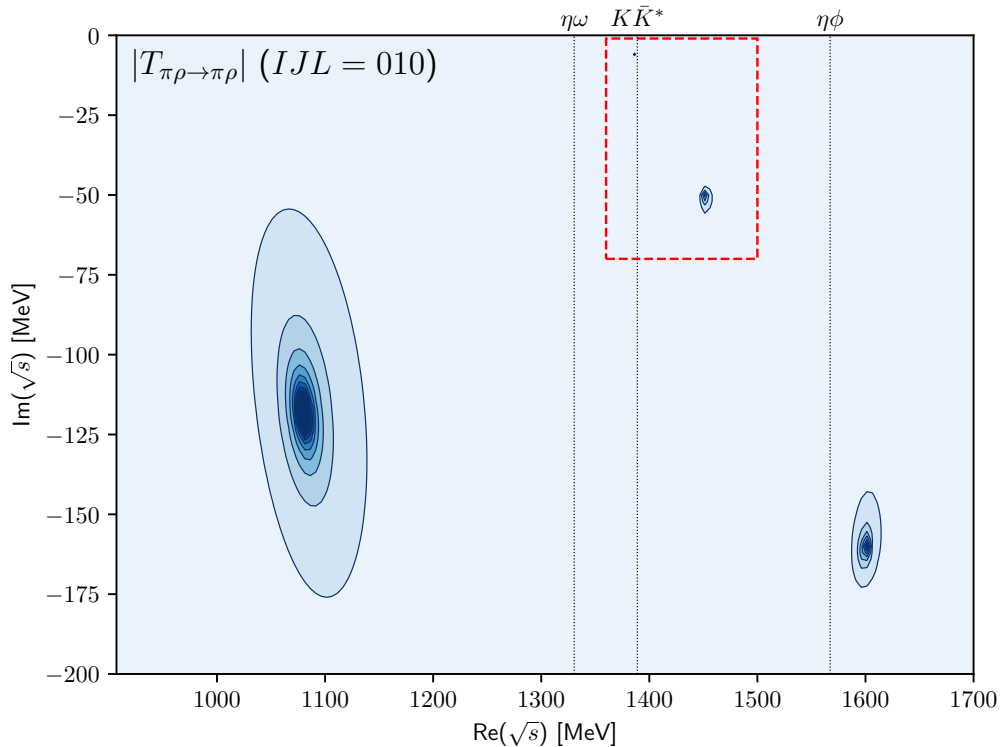
Figure 5. Contour plot of the modulus of the $\pi\rho$ transition amplitude in the complex $\sqrt{s}$ plane. Four poles are found in the second Riemann sheet. The contour plot in the red rectangle is enlarged and shown in Fig. 6.

The coupling strengths of the h_1 resonances can be derived from the residues of the $\mathcal{T}$ matrix, defined as

$$\mathcal{R}_{a,b} := \lim_{s \to s_R} (s - s_R) \mathcal{T}_{a,b}/4\pi = g_a g_b. \tag{22}$$

It is impossible to determine the signs of the coupling strengths, so we choose the coupling strengths to the $\pi\rho$ channel to be positive. Then, we can determine the relative signs for other coupling strengths. Table II lists the results for the coupling strengths to all possible channels. The first resonance, $h_1(1170)$, couples most strongly to

Table II. Coupling strengths in units of GeV of the h_1 resonance to the S and D wave states in the six different channels. Note that we fix the relative signs of the coupling strengths choosing the coupling strengths to the $\pi\rho$ channel to be positive.

$\sqrt{s_R}$ [MeV]	$1080 - i118$	$1387 - i6$	$1452 - i51$	$1603 - i158$
$g_{\pi\rho}(S\text{-wave})$	$4.23 - i1.80$	$0.43 + i0.20$	$0.85 - i1.37$	$2.81 + i0.28$
$g_{\pi\rho}(D\text{-wave})$	$0.48 - i0.42$	$0.18 + i0.17$	$1.09 + i0.11$	$1.51 - i0.15$
$g_{\eta\omega}(S\text{-wave})$	$-1.05 + i0.87$	$1.74 + i0.49$	$1.69 + i1.49$	$2.42 - i2.01$
$g_{\eta\omega}(D\text{-wave})$	$-0.12 + i0.03$	$-0.09 - i0.02$	$-0.19 - i0.01$	$-0.77 + i0.80$
$g_{K\bar{K}^*}(S\text{-wave})$	$-0.47 + i0.12$	$-4.23 - i0.95$	$-1.20 - i2.74$	$1.92 - i0.80$
$g_{K\bar{K}^*}(D\text{-wave})$	$-0.04 - i0.01$	$0.00 + i0.01$	$-0.21 + i0.50$	$-1.78 + i0.32$
$g_{\eta\phi}(S\text{-wave})$	$-3.96 + i0.79$	$4.84 + i1.23$	$8.83 + i1.52$	$0.04 + i4.12$
$g_{\eta\phi}(D\text{-wave})$	$-0.51 - i0.03$	$-0.21 - i0.06$	$-0.22 - i0.15$	$-0.42 + i0.43$
$g_{\eta'\omega}(S\text{-wave})$	$-0.74 + i0.69$	$-0.06 + i0.19$	$1.26 + i0.23$	$2.51 - i0.95$
$g_{\eta'\omega}(D\text{-wave})$	$-0.20 + i0.12$	$0.01 - i0.02$	$-0.11 - i0.04$	$-0.15 - i0.09$
$g_{\eta'\phi}(S\text{-wave})$	$0.66 - i0.13$	$-1.52 - i0.31$	$-1.83 - i0.67$	$0.30 - i0.67$
$g_{\eta'\phi}(D\text{-wave})$	$0.16 - i0.01$	$0.23 + i0.05$	$0.23 + i0.11$	$-0.05 + i0.05$

the $\pi\rho$ channel, which is in line with the experimental observations of the $h_1(1170) \to \pi\rho$ decay [28, 29, 33]. The next strongest coupling comes from the $\eta\phi$ channel. Considering that the $\eta\phi$ threshold energy is around 1570 MeV, it is remarkable that the $\eta\phi$ channel is the second most dominant one for $h_1(1170)$. This indicates that the $h_1(1170)$ contains a significant $s\bar{s}$ component, resembling the case of dynamically generated $a_1(1260)$ and $b_1(1235)$ [11, 12]. The

$\eta\phi$ channel couples most strongly to the second and third resonances, located at $(1387-i6)$ MeV and $(1452-i51)$ MeV, which are considered to be $h_1(1415)$. As depicted in Fig. 6, one can clearly observe the strongest peak structure below the $K\bar{K}^*$ threshold in the squared modulus of the $\eta\phi \to \eta\phi$ transition amplitude multiplied by $q_{\pi\rho}$, $q_{\pi\rho}|T|^2$, where $q_{\pi\rho}$ is the magnitude of the momentum of the $\pi\rho$ system. Interestingly, we also have nonvanishing $\pi\rho \to \eta\phi$ transition amplitudes, as shown in Fig. 6. Although we impose the flavor SU(3) symmetry, which results in the absence of the $\pi\rho \to \eta\phi$ kernel amplitude, the $\pi\rho \to \eta\phi$ transition amplitude is generated through the $K\bar{K}^*$ intermediate states, revealing a resonance structure below the $K\bar{K}^*$ threshold. As expected, the second resonance has a strong coupling strength to the $K\bar{K}^*$ channel (see also the dash-dotted curve in Fig. 6). On the other hand, the coupling strengths to the S-wave $\eta\omega$, $K\bar{K}^*$, $\eta'\omega$, and $\eta'\phi$ channels are of the same order. It is worth noting that the D-wave $\pi\rho$ channel has a sizable coupling strength. As for the $h_1(1595)$, many channels are strongly coupled to it. As explained eralier,
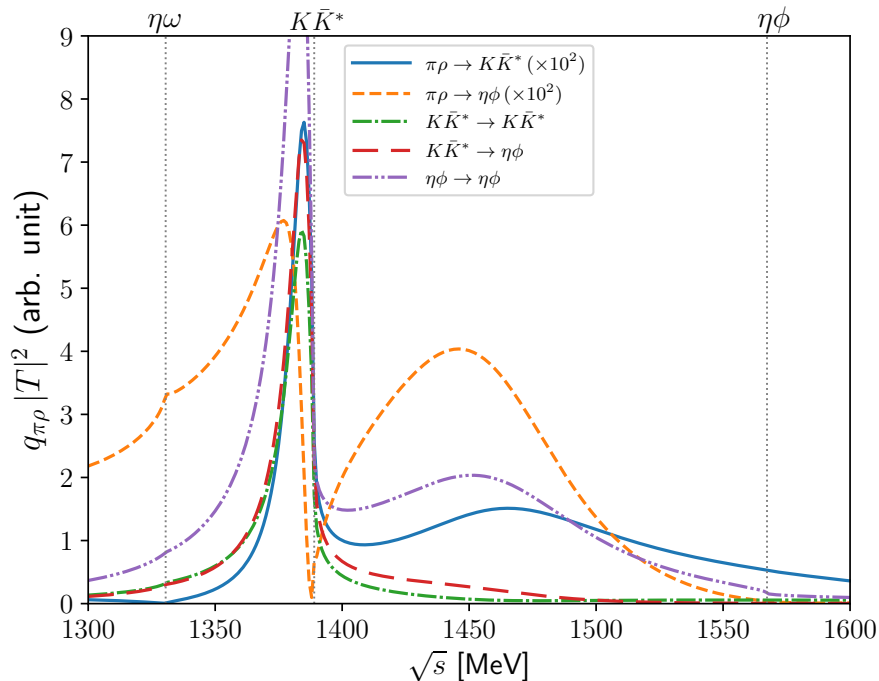

Figure 6. Results for $q_{\pi\rho}|T|^2$ for various channels. $q_{\pi\rho}$ is the magnitude of the momentum of the $\pi\rho$ system.

the mass of $h_1(1595)$ would have been less than the bare mass had we considered the $\pi\rho$ channel only. As shown in Table II, the $\pi\rho$, $\eta\omega$, $K\bar{K}^*$, and $\eta'\omega$ contribute to the generation of the $h_1(1595)$ meson.

B. Two-pole structure of the $h_1(1415)$

Table III. The experimental results on the mass and width of $h_1(1415)$ from various collaborations.

Collaboration	Reference	Process	Mass [MeV]	Width [MeV]
LASS	[2]	$K^-p \to K_S^0\bar{K}\pi\Lambda$	1380 ± 20	80 ± 30
Crystal Barrel	[3]	$p\bar{p} \to K_L K_S \pi^0\pi^0$	1440 ± 60	170 ± 80
BESIII	[4]	$\chi_{1,2,J} \to \phi K\bar{K}\pi$	1412 ± 12	84 ± 52
BESIII	[5]	$J/\psi \to \eta' K\bar{K}\pi$	1423.2 ± 9.4	90.3 ± 27.3
			$1441.7 \pm 4.9^{(*)}$	$111.5 \pm 12.8^{(*)}$
BESIII	[1]	$J/\psi \to \gamma\eta'\eta'$	$1384 \pm 6^{+9}_{-0}$	$66 \pm 10^{+12}_{-10}$

$^{(*)}$Interference effect is considered

Table III presents the mass of the $h_1(1415)$ as measured by various experiments. The LASS Collaboration initially detected a signal of $h_1(1415)$ in the $K\bar{K}\pi$ system using the $K^-p \to K_S^0\bar{K}\pi\Lambda$ reaction [2]. The data exhibited an enhancement near 1.4 GeV, diminishing rapidly as the energy increased. Using the Breit-Wigner parameterization, the

mass and width were determined to be $M = 1380\pm20$ MeV and $\Gamma = 80\pm30$ MeV, respectively. Subsequent experiments, however, reported different results. The Crystal Barrel Collaboration [3] performed proton annihilation to produce the $K\bar{K}\pi$ system and discovered the h_1 meson above the $K\bar{K}^*$ threshold, with a mass of $M = (1440 \pm 60)$ MeV and a width of $\Gamma = (170 \pm 80)$ MeV. Two experimental results from the BESIII Collaboration, obtained from different charmonium state decays, confirmed these findings with a slightly lower mass. It is noteworthy that interference influences the determination of the mass and width of the $h_1(1415)$ [5], and these results align with those of the Crystal Barrel experiment. In a recent experiment conducted by the BESIII [1] Collaboration, the mass and width of the $h_1(1415)$, measured in the $\gamma\eta'$ invariant mass, were found to be consistent with those obtained by the LASS Collaboration but contradictory to the two previous BESIII results. This discrepancy strongly suggests that the $h_1(1415)$ does not originate from a single pole, indicating a more complex structure. Evidently, this structure cannot be explained by the quark model alone. Consequently, based on the results of this study, we propose a two-pole structure to account for the discrepancy in the measurements of the $h_1(1415)$ meson mass.
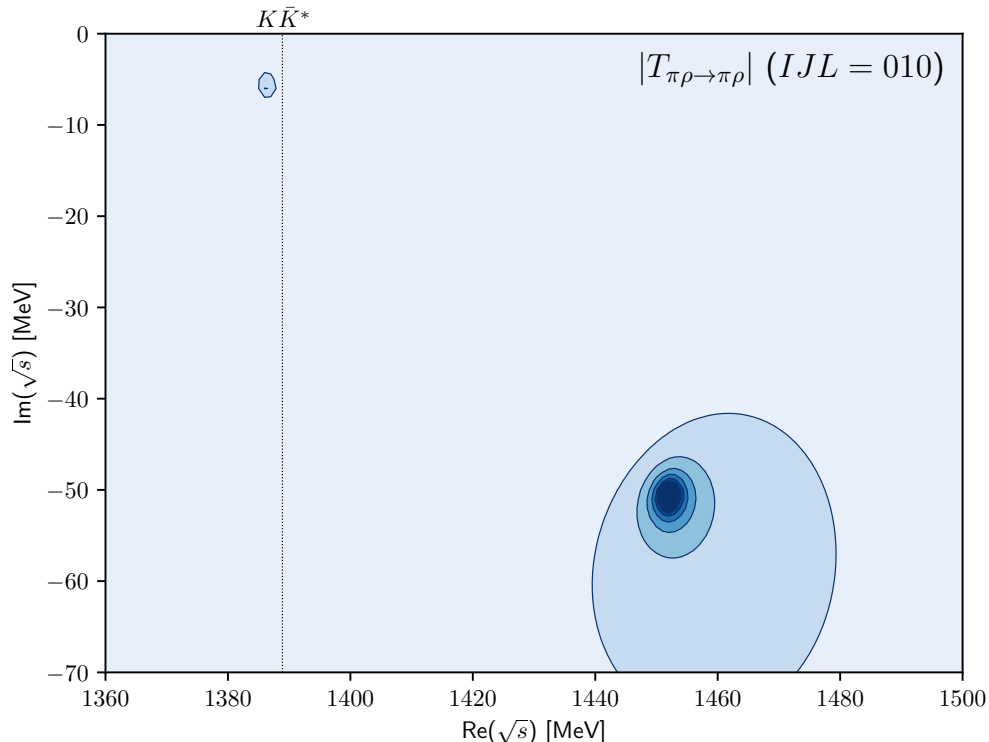

Figure 7. Contour plot of $\pi\rho \to \pi\rho$ transition amplitude in the complex $\sqrt{s}$ plane, which enlarges the red rectangle in Fig. 5.

The current work reveals two poles around 1.4 GeV, one at $(1387 - i6)$ MeV and the other at $(1452 - i51)$ MeV, as shown in Table II. Figure 7 demonstrates how these two poles appear in the complex energy plane. The lower pole is located close to the $K\bar{K}^*$ threshold, while the higher pole is situated 80 MeV above it. Due to its narrowness, detecting the lower pole experimentally may pose a challenge. Examining the coupling strengths in Table II, we observe that both poles couple strongly to open strange and hidden strange channels. However, the higher pole couples to the $\eta\phi$ channel far more strongly than to other channels. This suggests that the higher pole might be an $\eta\phi$ molecular state, while the lower pole, being located very close to the $K\bar{K}^*$ threshold, could be a $K\bar{K}^*$ molecular state. Notably, the $g_{K\bar{K}^*}$ for the higher pole has a larger imaginary part than its real part, causing destructive interference. This results in the disappearance of the higher pole in $K\bar{K}^*$ elastic scattering, a feature also observed in the case of the higher pole of the b_1 meson in a previous study [12]. This characteristic is the essential clue to explaining the absence of the higher pole in the LASS Collaboration experiment.

Based on this analysis, we propose an explanation for the conflicting mass measurements of $h_1(1415)$. As shown in Fig. 6, the crucial aspect is that the higher pole vanishes in $K\bar{K}^*$ elastic scattering, leaving only the $K\bar{K}^*$ threshold enhancement. The LASS collaboration investigated the $h_1(1415)$ in the $K^-p \to K_S^0\bar{K}\pi\Lambda$ process, which can effectively be represented as $K\bar{K}^*$ elastic scattering. They observed a threshold enhancement near the $K\bar{K}^*$ threshold, aligning with the current results. In contrast, the Crystal Barrel [3] and BESIII experiments [4, 5] measured the $K\bar{K}\pi$ state as a final state, which can be considered as the $K\bar{K}^*$ state. Consequently, both collaborations measured the $h_1(1415)$

above the $K\bar{K}^*$ threshold. The most recent measurement from the BESIII Collaboration comes from the $J/\psi \to \gamma\eta'\eta'$ decay. In conclusion, we propose that the $h_1(1415)$ can be constructed from two different resonances: the $h_1(1380)$ and $h_1(1440)$ mesons, with the higher pole vanishing in $K\bar{K}^*$ elastic scattering. This two-pole structure accounts for the seemingly conflicting experimental results.

IV. SUMMARY AND CONCLUSIONS

In this work, we aimed at investigating the isoscalar axial-vector h_1 mesons using a coupled-channel formalism. We first constructed kernel amplitudes from meson-exchange diagrams in the t- and u-channels, derived from effective Lagrangians based on hidden local symmetry. In addition, we introduced the pole diagram for $h_1(1595)$ to generate the $h_1(1595)$ resonance. We found that the $h_1(1595)$ pole diagram also has a significant effect on the generation of $h_1(1170)$. Six channels were incorporated: $\pi\rho$, $\eta\omega$, $K\bar{K}^*$, $\eta\phi$, $\eta'\omega$, and $\eta'\phi$ channels. We solved the off-shell coupled integral equations and discussed the dynamical generation of the $h_1(1170)$. The present analysis revealed two poles at $(1387 - i6)$ MeV and $(1452 - i51)$ MeV, exhibiting a two-pole structure of the $h_1(1415)$ meson. This two-pole structure may resolve the discrepancy in the experimental data on the mass of $h_1(1415)$. The results showed that the lower pole couples strongly to the $K\bar{K}^*$ channel, while the higher pole couples predominantly to the $\eta\phi$ channel. This provides an essential clue to understand the nature of h_1 mesons and explains possible discrepancies in the mass of $h_1(1415)$. The two-pole structure of $h_1(1415)$ can account for the seemingly conflicting experimental results, with the lower pole corresponding to $h_1(1380)$ and the higher pole to $h_1(1440)$. Notably, the higher pole vanishes in $K\bar{K}^*$ elastic scattering, which explains why some experiments observe only the lower pole.

ACKNOWLEDGMENTS

[1] M. Ablikim *et al.* (BESIII), Phys. Rev. D **105**, 072002 (2022), arXiv:2201.09710 [hep-ex].
[2] D. Aston *et al.* (LASS), Phys. Lett. B **201**, 573 (1988).
[3] A. Abele *et al.* (Crystal Barrel), Phys. Lett. B **415**, 280 (1997).
[4] M. Ablikim *et al.* (BESIII), Phys. Rev. D **91**, 112008 (2015), arXiv:1503.04699 [hep-ex].
[5] M. Ablikim *et al.* (BESIII), Phys. Rev. D **98**, 072005 (2018), arXiv:1804.05536 [hep-ex].
[6] S. Navas *et al.* (Particle Data Group), Phys. Review D **110**, 030001 (2024).
[7] J. L. Basdevant and E. L. Berger, Phys. Rev. D **16**, 657 (1977).
[8] L. Roca, E. Oset, and J. Singh, Phys. Rev. D **72**, 014002 (2005), arXiv:hep-ph/0503273.
[9] M. F. M. Lutz and E. E. Kolomeitsev, Nucl. Phys. A **730**, 392 (2004), arXiv:nucl-th/0307039.
[10] H. Nagahiro, K. Nawa, S. Ozaki, D. Jido, and A. Hosaka, Phys. Rev. D **83**, 111504 (2011), arXiv:1101.3623 [hep-ph].
[11] S. Clymton and H.-C. Kim, Phys. Rev. D **106**, 114015 (2022), arXiv:2208.04124 [hep-ph].
[12] S. Clymton and H.-C. Kim, Phys. Rev. D **108**, 074021 (2023), arXiv:2305.14812 [hep-ph].
[13] L. S. Geng, E. Oset, L. Roca, and J. A. Oller, Phys. Rev. D **75**, 014017 (2007), arXiv:hep-ph/0610217.
[14] M. Albaladejo, P. Fernandez-Soler, F.-K. Guo, and J. Nieves, Phys. Lett. B **767**, 465 (2017), arXiv:1610.06727 [hep-ph].
[15] U.-G. Meißner, Symmetry **12**, 981 (2020), arXiv:2005.06909 [hep-ph].
[16] J. A. Oller and U. G. Meissner, Phys. Lett. B **500**, 263 (2001), arXiv:hep-ph/0011146.
[17] D. Jido, J. A. Oller, E. Oset, A. Ramos, and U. G. Meissner, Nucl. Phys. A **725**, 181 (2003), arXiv:nucl-th/0303062.
[18] J.-M. Xie, J.-X. Lu, L.-S. Geng, and B.-S. Zou, Phys. Rev. D **108**, L111502 (2023), arXiv:2307.11631 [hep-ph].
[19] H.-J. Kim and H.-C. Kim, Prog. Theo. Exp. Phys **2024**, 073D01 (2024).
[20] R. Blankenbecler and R. Sugar, Phys. Rev. **142**, 1051 (1966).
[21] R. Aaron, R. D. Amado, and J. E. Young, Phys. Rev. **174**, 2022 (1968).
[22] S. Clymton, H.-C. Kim, and T. Mart, (2024), arXiv:2408.04166 [hep-ph].
[23] T. Fujiwara, T. Kugo, H. Terao, S. Uehara, and K. Yamawaki, Prog. Theor. Phys. **73**, 926 (1985).
[24] M. Bando, T. Kugo, and K. Yamawaki, Phys. Rept. **164**, 217 (1988).
[25] C. Amsler and F. E. Close, Phys. Rev. D **53**, 295 (1996), arXiv:hep-ph/9507326.
[26] H.-C. Kim, J. W. Durso, and K. Holinde, Phys. Rev. C **49**, 2355 (1994).
[27] D. Lohse, J. W. Durso, K. Holinde, and J. Speth, Nucl. Phys. A **516**, 513 (1990).
[28] J. A. Dankowych *et al.*, Phys. Rev. Lett. **46**, 580 (1981).
[29] A. Ando *et al.*, Phys. Lett. B **291**, 496 (1992).

[30] P. Eugenio *et al.* (BNL-E852), Phys. Lett. B **497**, 190 (2001), arXiv:hep-ph/0010337.

[31] G. Janssen, K. Holinde, and J. Speth, Phys. Rev. C **54**, 2218 (1996).

[32] Z. Zhao, K. Xu, A. Kaewsnod, X. Liu, A. Limphirat, and Y. Yan, Phys. Rev. D **105**, 036001 (2022), arXiv:2108.06155 [hep-ph].

[33] M. Atkinson *et al.* (Omega Photon), Nucl. Phys. B **243**, 1 (1984).